

# Recycling of Plastic Wastes for Mass Production of Yolk-Shell Nanostructured $\text{Co}_3\text{O}_4@\text{C}$ for Lithium-Ion Batteries

Jiaxin Lia <sup>a§</sup>, Fei Dou <sup>b§</sup>, Jiang Gong <sup>c</sup>, Yanshen Gao <sup>a</sup>, Yumeng Hua <sup>d</sup>, Krzysztof Sielicki <sup>a</sup>, Dengsong Zhang <sup>b,\*</sup>, Ewa Mijowska <sup>a</sup>, Xuecheng Chen <sup>a\*</sup>

<sup>a</sup> Faculty of Chemical Technology and Engineering, West Pomeranian University of Technology, Szczecin, Piastów Ave. 42, Szczecin 71-065, Poland.

<sup>b</sup> School of Materials Science and Engineering & Research Center of Nano Science and Technology, Shanghai University, Jufengyuan Rd, Baoshan, Shanghai, 200444, China.

<sup>c</sup> Key Laboratory of Material Chemistry for Energy Conversion and Storage, Ministry of Education, School of Chemistry and Chemical Engineering, Huazhong University of Science and Technology, Luoyu Rd, Hongshan, Wuhan 430074, China.

<sup>d</sup> School of Environment and Chemical Engineering, Shenyang University of Technology, Shenyang 110870, China.

§J. L. and F. D contributed equally to this paper.

\*E-mail: xchen@zut.edu.pl (X. Chen); dszhang@shu.edu.cn (D. Zhang);

KEYWORDS: waste plastic; face mask; yolk-shell structure;  $\text{Co}_3\text{O}_4/\text{C}$  composite; lithium-ion battery

**ABSTRACT:** Facing the ever-increasing production of municipal plastics, great efforts have been made to recycle plastic waste into high value-added products. As the main components of plastic wastes, PP, PE and PS are uncharred polymers, which are hard to be carbonized under normal conditions. To address this issue, transition metal catalysts ( $\text{Co}_3\text{O}_4$ ) were introduced to carbonize the plastic waste with high carbon yields. Herein, the mixed waste plastics (PP/PE/PS) were carbonized into yolk-shell structured  $\text{Co}_3\text{O}_4$ @carbon nanomaterials with high yield of 49 wt%. A high capacity of 1066 mAh  $\text{g}^{-1}$  at 0.1 A  $\text{g}^{-1}$  after 100 cycles in lithium-ion batteries. Moreover, the galvanostatic intermittent titration technique (GITT) results estimated that the YSS  $\text{Co}_3\text{O}_4$ @C possessed a higher  $\text{Li}^+$  diffusion coefficient, ensuring an improved cycling stability and rate performance. The present strategy not only provides a potential approach for recycling waste plastics into high-value carbon materials, but also shows the possibility for the mass production of high-performance nanosized anode materials for LIBs in a commercial way.

## **Introduction**

Over the past decades, plastic products have brought considerable convenience to our daily life due to their lightweight, high chemical stability and low degradability, such as polyethylene (PE), polypropylene (PP) and polystyrene (PS).<sup>1</sup> For example, face masks have become the most common and important personal protective equipment during the worldwide pandemic Coronavirus Disease 2019 (COVID-19), which are mainly consisted of PP as

the protective layers. Consequently, millions of masks are consumed every day without recycling, which could severely pose plastic pollution.<sup>2-3</sup> The traditional options for treating the waste plastics are landfilling and incineration, which have shown serious concern due to potential environmental pollution. Consequently, it is urgent to explore economic beneficial and practical methods to recycle the waste plastics into high value-added materials.<sup>4</sup>

Among the reported recycling strategies, chemical recycling has attracted great attention because it followed the principle of “sustainable development”, which can convert polymers into smaller organic molecules for further applications.<sup>5-6</sup> However, it is still a challenge to develop facile and cost-effective approaches to transform plastics wastes into targeted products. Considering the high carbon content of plastic wastes, such as PE, PP and PS, converting plastic waste into high valued-added carbon materials is regarded as one of the great choices for recycling plastic wastes.<sup>7-8</sup> However, PP, PE and PS are uncharred polymers, which are hard to be carbonized in the traditional way<sup>9-10</sup>. To address this issue, transition metal catalysts were selectively introduced to highly carbonize the plastic waste with high yields.<sup>11-12</sup> More importantly, it is still challenging to fully make use of the obtained products (carbon materials/metal nanoparticles) in a proper way.

Lithium-ion batteries (LIBs) are highly needed in portable consumer electronics, electronic vehicles, emerging wearable devices, *etc*, due to their high energy density, cycling stability and low cost.<sup>13-14</sup> Graphite is the most

conventional anode material for LIBs, which only show a theoretical capacity of 372 mAh g<sup>-1</sup>, which can not meet the exceptional demands for high volumetric and gravimetric energy density of the next generation LIBs<sup>15</sup>. Co<sub>3</sub>O<sub>4</sub> is attractive due to its high specific theoretical capacity (890 mAh g<sup>-1</sup>), natural abundance and eco-friendly properties. However, the commercial application of Co<sub>3</sub>O<sub>4</sub> is limited by electrochemical instability caused by the large volume change during charge/discharge processes and sluggish reaction kinetics caused by its low intrinsic electronic conductivity.<sup>16-17</sup> Recently, several strategies have been proposed to solve these problems. It is reported that the nanometer-sized Co<sub>3</sub>O<sub>4</sub> showed decreased volume change due to the nano-effect, but some of the challenges related to low electronic conductivity can't completely alleviate.<sup>18</sup> The Co<sub>3</sub>O<sub>4</sub> nanoparticles with various morphologies were embedded into highly electrical conductivity carbon materials, such as graphene, carbon nanotubes (CNTs) and MXene,<sup>19-21</sup> which has been shown to be effective to address these issues. Unfortunately, the long-term cycling stability is still unsatisfactory for practical application, which caused the inevitable structural pulverization and volume change.

In this work, a simple and effective method was proposed for the recycling of plastic wastes into nanosized yolk-shell structured (YSS) Co<sub>3</sub>O<sub>4</sub>@C for LIBs via catalytic carbonization followed partially etching of the Co<sub>3</sub>O<sub>4</sub>. The mixed plastic from life was used as carbon source including waste mask (PP), waste plastic jar (PE) and foam sheets (PS), by use of Co<sub>3</sub>O<sub>4</sub> nanoparticles as the

catalyst for carbonization and as the supporting material for Li<sup>+</sup> ion storage. Moreover, a void space located at the inner core of Co<sub>3</sub>O<sub>4</sub> and outer carbon layer was obtained via partial etching of the active materials, which can release the stress caused by repeated lithiation/delithiation cycles and result in improved electrochemical stability. These features have greatly improved the electrode kinetics and promoted a highly reversible reaction process in the investigated long-term cyclic process. The nanosized YSS Co<sub>3</sub>O<sub>4</sub>@C exhibited a high capacity of 1066 mAh g<sup>-1</sup> at 0.1 A g<sup>-1</sup> after 100 charge/discharge cycles, and excellent of cycle performance. The conversion of waste plastics into the nanosized YSS Co<sub>3</sub>O<sub>4</sub>@C not only provides a new method for the mass production of t high performance electrode materials for LIBs, but also concepts an effective way for recycling of the waste polymers from daily life.

## **Experimental Section**

### *Materials*

Waste plastics were collected from daily life, including the waste face mask (PP), plastic jar (PE) and foam sheets (PS). The nanosphere Co<sub>3</sub>O<sub>4</sub> (analytical grade) was purchased from Sinopharm Chemical Reagents Co., Ltd., China. HCl was obtained from Sigma-Aldrich Chemical Co. All chemicals were analytical grade and used as received.

### *Synthesis of mixed plastics-Co<sub>3</sub>O<sub>4</sub> composite (P-Co<sub>3</sub>O<sub>4</sub>)*

The waste plastics were cut into small pieces (1 cm \* 1 cm) after washing and drying. The Co<sub>3</sub>O<sub>4</sub> (37 wt%) was mixed with the mixture of different plastic

(35g) consisting of PP (17 wt%), PE (35 wt%) and PS (11 wt%) in a Brabender mixer at 100 rpm and 180 °C for 10 min, and the resulting sample was named as P-Co<sub>3</sub>O<sub>4</sub>.

#### *Synthesis of the nanosized core-shell structured (CSS) Co@C nanoparticles*

The nanosized CSS Co@C nanoparticles were obtained via the carbonization process by heating the P-Co<sub>3</sub>O<sub>4</sub> at 700 °C. In a typical experiment, a piece of P-Co<sub>3</sub>O<sub>4</sub> (about 5 g) was annealed at 700 °C for 6 min. The obtained black powder was cooled down to room temperature and named the CSS Co@C.

#### *Synthesis of nanosized CSS Co<sub>3</sub>O<sub>4</sub>@C and yolk-shell structured (YSS) Co<sub>3</sub>O<sub>4</sub>@C*

The nanosized CSS Co@C (0.5 g) was placed in the tube furnace and heating at 280 °C in the air at a heated rate of 10 °C min<sup>-1</sup> for complete oxidization of Co to Co<sub>3</sub>O<sub>4</sub>, followed by cooling down to the room temperature naturally. A certain amount of the nanosized CSS Co<sub>3</sub>O<sub>4</sub>@C was dispersed in 2M HCl solution for a certain time to partially etch the Co<sub>3</sub>O<sub>4</sub> to obtain the nanosized YSS Co<sub>3</sub>O<sub>4</sub>@C followed by membrane filtration, washing with water, and drying at 100 °C in vacuum oven over night.

#### *Characterizations*

The transmission electron microscopy (TEM, JEM-1011at 100 kV) and field emission scanning electron microscope (SEM, XL30ESEM-FEG, accelerating voltage at 100 kV) equipped with energy dispersive X-ray mapping were used

to observe the microstructure, morphology and surface element distribution. To analyze the crystal structure of samples, powder X-ray diffraction (XRD) patterns were recorded on a D8 Advance X-ray diffractometer with Cu-K $\alpha$  radiation. Raman spectrum was performed on a Renishaw micro-Raman spectrometer. The thermal stability and content of the Co<sub>3</sub>O<sub>4</sub> in its composites were determined by thermal gravimetric analysis (TGA) under air flow at a heating rate of 10°C/min using a TA Instruments SDT Q600. X-ray photoelectron spectroscopy (XPS, VG ESCALABMK II spectrometer) was performed to record the surface element data of the samples with Al K $\alpha$  radiation excitation source at 10.0 kV and 10 mA. N<sub>2</sub> isotherms were obtained at -196°C on the Quantachrome Autosorb-1C-MS analyzer. The Brunauer-Emmett-Teller (BET) method and density functional theory (DFT) were utilized to calculate the specific surface area and pore size distribution of the CSS Co<sub>3</sub>O<sub>4</sub>@C and YSS Co<sub>3</sub>O<sub>4</sub>@C nanoparticles.

#### *Electrochemical measurements*

The slurry contained active materials, Super-P and carboxymethyl cellulose (CMC) in N, N-dimethylformamide solution with a weight ratio of 8:1:1 was casted on the Cu foil, followed by drying at 150 °C in vacuum oven overnight to remove the solvent. The mass loading was 1-1.5 mg cm<sup>-2</sup>. Then the Cu foil was cut into 15 mm wafers on a slicing machinery. The CR2032-type cells with Li foil and 1M LiPF<sub>6</sub> in EC: EMC (1:2 w/w) were respectively employed as the reference electrode and electrolytes were assembled in an argon-filled

glovebox (O<sub>2</sub> and H<sub>2</sub>O contents <1 ppm). The electrochemical performance was evaluated in the voltage range of 0.005-3.0 V by use of galvanostatic charge/discharge at a scan rate of 0.1 A g<sup>-1</sup>. Cyclic voltammetry (CV) was performed on an electrochemical workstation (CHI 660D) from 0.005 to 3.0 V at a scan rate of from 0.1 mV s<sup>-1</sup> to 1.0 mV s<sup>-1</sup>. Long term performance and rate performance was tested based on the galvanostatic charge/discharge technique at different current density (0.1 A g<sup>-1</sup> to 5 A g<sup>-1</sup>) with a certain cycle number with BioLogic Science Instruments (EC-LAB VPM3). Electrochemical impedance spectroscopy (EIS) measurements were carried out in a frequency window of 1 MHz-0.01 Hz with electrochemical workstation (CHI 660D). The impedance fitting was accomplished by Zview software, limiting the systematic error of the calculation to under 10%. The galvanostatic intermittent titration technique (GITT) measurement was conducted by applying a galvanostatic current of 0.02 A g<sup>-1</sup> within 0.005-3V on the EC-LAB VPM3.

The diffusion coefficient ( $D$ , cm<sup>2</sup> s<sup>-1</sup>) is calculated according to Eq. (1) <sup>22</sup>

$$D = R^2 T^2 / 2 A^2 n^4 F^4 C^2 \sigma^2 \quad (1)$$

where  $R$  is the universal gas constant,  $T$  is the absolute temperature,  $F$  is the Faraday constant,  $A$  is the electrode area, and  $n$  is the number of electrons per molecule Co<sub>3</sub>O<sub>4</sub> during the discharge/charge process,  $C$  is the concentration of lithium ions in the electrode, and  $\sigma$  is the Warburg factor which has a relationship with the real part of impedance ( $Z'$ ), the resistance of electrolyte

and cell ohmic ( $R_s$ ), charge transfer resistance ( $R_{ct}$ ), and angular frequency ( $\omega$ ).

23

$$Z' = R_s + R_{ct} + \sigma \frac{1}{\sqrt{\omega}} \quad (2)$$

## Results and discussion

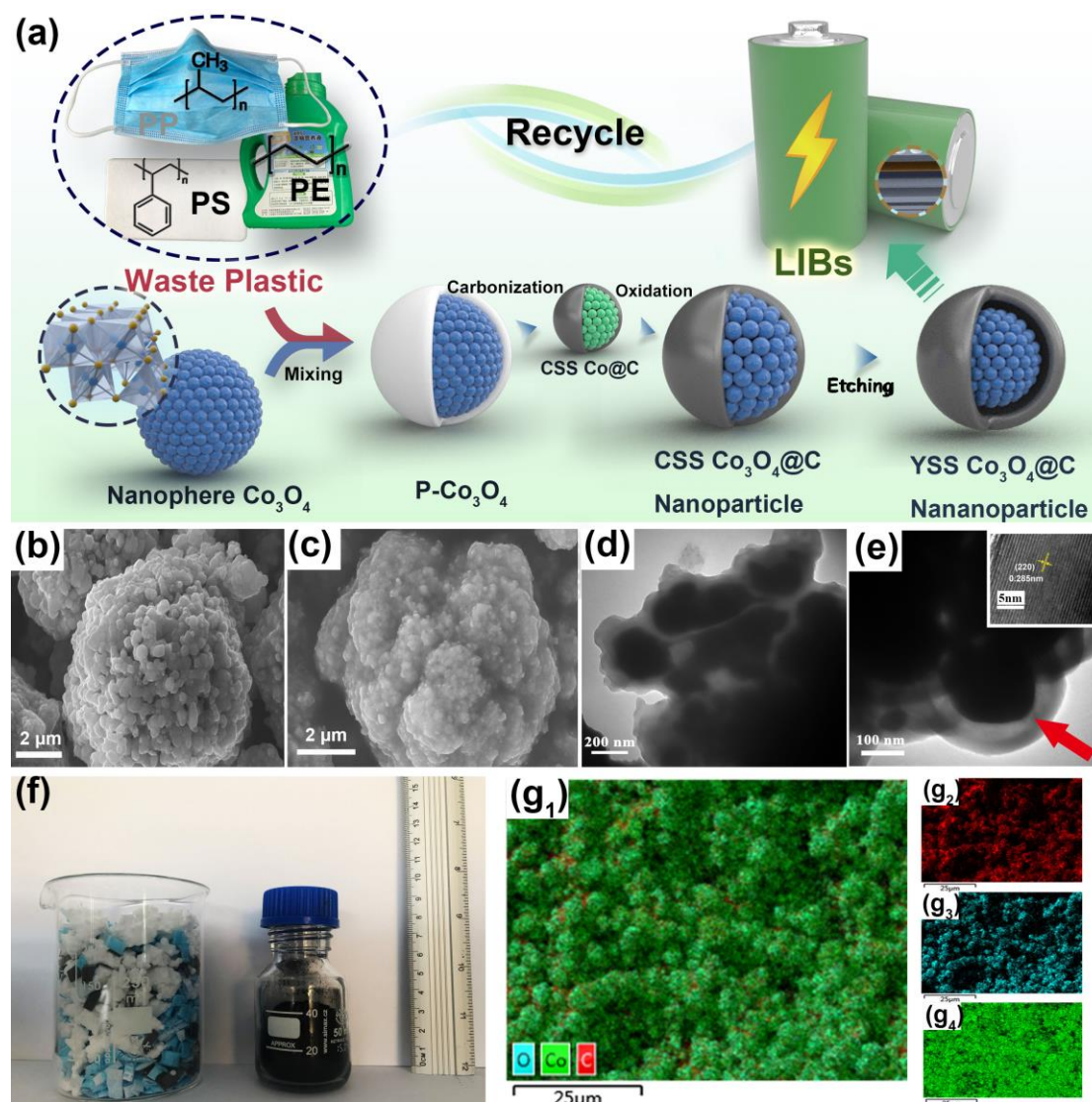


**Figure 1.** (a) Schematic diagram for preparation of nanosized YSS  $\text{Co}_3\text{O}_4@\text{C}$ . SEM images of (b) Nanosphere  $\text{Co}_3\text{O}_4$ ; (c) P- $\text{Co}_3\text{O}_4$ . TEM images of (d) CSS  $\text{Co}_3\text{O}_4@\text{C}$  nanoparticles and (e) YSS  $\text{Co}_3\text{O}_4@\text{C}$  nanoparticles (void space was marked by red arrow; inset: lattice spacing of (220) plane). (f) Photographs of

waste plastics (left) and YSS  $\text{Co}_3\text{O}_4@\text{C}$  materials (right). (g<sub>1</sub>) EDX mapping of YSS  $\text{Co}_3\text{O}_4@\text{C}$  nanoparticles: (g<sub>2</sub>) carbon; (g<sub>3</sub>) oxygen and (g<sub>4</sub>) cobalt element.

The preparation of the YSS  $\text{Co}_3\text{O}_4@\text{C}$  nanoparticles was illustrated in **Figure 1a** and which consist of three steps. Firstly, the CSS  $\text{Co}@\text{C}$  nanoparticles were prepared by catalytic carbonization of the mixed plastics using the  $\text{Co}_3\text{O}_4$  nanoparticles as the catalysts. Subsequently, annealing of the obtained CSS  $\text{Co}@\text{C}$  nanoparticles in air yielded the CSS  $\text{Co}_3\text{O}_4@\text{C}$  nanoparticles. After partial etching of the  $\text{Co}_3\text{O}_4$  with 2M HCl acid, a void space located between the carbon layer and  $\text{Co}_3\text{O}_4$  nanoparticles was obtained, resulting in the YSS  $\text{Co}_3\text{O}_4@\text{C}$  nanoparticles, which was used as the anode material for LIBs. The morphology and nanostructure of waste plastic derived composites (Nanosphere  $\text{Co}_3\text{O}_4$ , P- $\text{Co}_3\text{O}_4$ , CSS  $\text{Co}@\text{C}$ , CSS  $\text{Co}_3\text{O}_4@\text{C}$  and YSS  $\text{Co}_3\text{O}_4@\text{C}$ ) were characterized by SEM and TEM. As shown in **Figure 1b** and **1c**, the sphere-liked  $\text{Co}_3\text{O}_4$  was completely encapsulated by the waste polymer after melt blending, as confirmed by the SEM and EDX mapping (**Figure S2** and **S3**). The CSS  $\text{Co}@\text{C}$  nanoparticles were obtained after catalytic carbonization of the plastic with  $\text{Co}_3\text{O}_4$  (**Figure 1d** and **Figure S4**). Based on the previous reports, the possible mechanism was proposed as following: the waste plastics were pyrolyzed into light hydrocarbons and aromatics under high temperature (**Figure S1**).<sup>8, 24</sup> The dehydrogenated and aromatized process reacted on the surface of  $\text{Co}_3\text{O}_4$  catalyst, meanwhile  $\text{Co}_3\text{O}_4$  was reduced into Co. The core/shell structural  $\text{Co}@\text{C}$  nanoparticles (CSS

Co@C) were obtained after the carbonization of the degradation produces. After completely oxidation process, all the Co nanoparticles were transferred into  $\text{Co}_3\text{O}_4$  nanoparticles without morphology distortion, as shown in **Figure 1d**. It is clear to see the void structure (30 nm) between the inner sphere  $\text{Co}_3\text{O}_4$  and out carbon layer is formed, as observed in **Figure 1e**. Furthermore, the lattice plane of (220) with d spacing of 0.285nm was confirmed in the inset of **Figure 1e**. In order to observe the yolk-shell structure with the void space, the over-etching was introduced, as shown in **Figure S5**. More importantly, the wastes plastics (PP, PE, PS) were carbonized into yolk-shell structured (YSS)  $\text{Co}_3\text{O}_4$ @carbon nanomaterials with high yield of 49 wt% by using  $\text{Co}_3\text{O}_4$  nanoparticles as the catalyst, higher than the single components of PP, PE or PS (**Figure 1f** and **Table S1**). The EDX mappings results further confirm the successful preparation of YSS  $\text{Co}_3\text{O}_4$ @C and that the C, Co, and O elements were homogeneously distributed (**Figure 1g**).

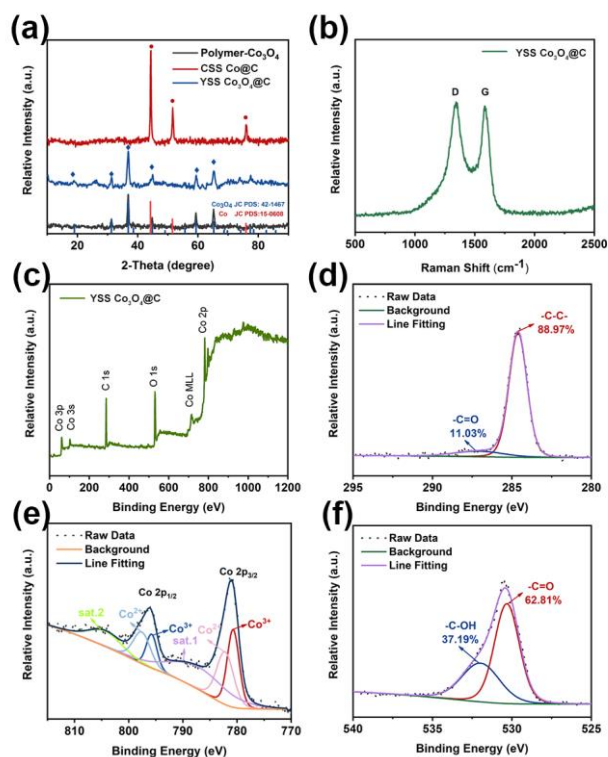


**Figure 2.** (a) XRD patterns of the P- $\text{Co}_3\text{O}_4$ , CSS Co@C nanoparticles, and YSS  $\text{Co}_3\text{O}_4$ @C nanoparticles. (b) Raman spectrum; (c) full XPS spectrum and high-resolution (d) C 1s, (e) Co 2p, and (f) O 1s XPS spectra of YSS  $\text{Co}_3\text{O}_4$ @C.

XRD analysis was employed to investigate the crystalline information of the P- $\text{Co}_3\text{O}_4$ , CSS Co@C, and YSS  $\text{Co}_3\text{O}_4$ @C nanoparticles in **Figure 2a**. Four sharp diffraction peaks ( $2\theta$ ) at  $31^\circ$ ,  $38^\circ$ ,  $59^\circ$  and  $65^\circ$  are respectively assigned to the (220), (222), (511) and (440) planes of the  $\text{Co}_3\text{O}_4$  in P- $\text{Co}_3\text{O}_4$  (according to JCPDS No. 42-1467).<sup>25</sup> The CSS Co@C nanoparticles exhibited three diffraction peaks at  $44^\circ$ ,  $51.5^\circ$  and  $75.8^\circ$  suggesting the (111), (200) and (220) planes of the cubic Co (according to JCPDS No. 15-0806).<sup>26</sup> After oxidization, these three peaks are completely replaced by the other four peaks ascribed to  $\text{Co}_3\text{O}_4$  in YSS  $\text{Co}_3\text{O}_4$ @C, indicating that metallic Co was completely oxidized into  $\text{Co}_3\text{O}_4$ . Moreover, the broader peak in YSS  $\text{Co}_3\text{O}_4$ @C nanoparticles than

that in P-Co<sub>3</sub>O<sub>4</sub> illustrates the etching process decreases the crystalline of Co<sub>3</sub>O<sub>4</sub>. The diffraction peaks of carbon are hardly to be observed due to the high relative intensity of the Co and Co<sub>3</sub>O<sub>4</sub>. The Raman spectra were recorded to estimate the graphitization of carbon layer. As shown in **Figure 2b**, the ratio of the intensity ( $I_D/I_G$ ) between the D band (1350 cm<sup>-1</sup>) and the G band (1580 cm<sup>-1</sup>) was used to estimate the structural defect the carbon material.<sup>27-28</sup> It is noted the value of  $I_D/I_G$  ratio was 1.15, implying large content of the defects in the carbon layer of the YSS Co<sub>3</sub>O<sub>4</sub>@C nanoparticles, which would benefit fast charge transportation in the electrolyte. TGA was used to evaluate the thermal stability and the contents of Co<sub>3</sub>O<sub>4</sub> in YSS Co<sub>3</sub>O<sub>4</sub>@C nanoparticles (**Figure S6**). The weight loss from 400 °C to 500 °C was attributed to the oxidation of carbon skeleton of graphite shells. The contents of Co<sub>3</sub>O<sub>4</sub> in YSS Co<sub>3</sub>O<sub>4</sub>@C nanoparticles was 29wt%, which renders from the weight percent of the residues at 900 °C.

The surface element and composition of the YSS Co<sub>3</sub>O<sub>4</sub>@C nanoparticles were further investigated by XPS. As shown in **Figure 2c**, the full XPS spectrum clearly showed the presence of carbon elements, cobalt elements and oxygen elements, which are located at 285 eV, 782 eV, and 531 eV, respectively.<sup>29-30</sup> High-resolution C 1s XPS spectrum (**Figure 2d**) showed two symmetric peaks at 284.62 eV and 287.08 eV, corresponding to the -C-C- and -C=O from carbon layer.<sup>31</sup> The Co 2p spectra of YSS Co<sub>3</sub>O<sub>4</sub>@C nanoparticles (**Figure 2e**) are consisted of Co 2p<sub>3/2</sub> and Co 2p<sub>1/2</sub>. One spin-orbit doublet of the Co 2p<sub>3/2</sub> can

be divided into two deconvoluted peaks of  $\text{Co}^{2+}$  (797.55 eV) and  $\text{Co}^{3+}$  (795.76 eV).<sup>32-33</sup> The characteristic peaks of the Co 2p<sub>1/2</sub> with binding energies of 780.79 eV and 782.50 eV are identified as the  $\text{Co}^{3+}$  and  $\text{Co}^{2+}$  species.<sup>34</sup> Additionally, the two weak peaks located at 786.28 eV and 804.33 eV are marked as sat. 1 and sat. 2, which can be attributed to the protruding satellite peaks of the Co 2p<sub>3/2</sub> and the Co 2p<sub>1/2</sub>, further indicating the existence of the  $\text{Co}_3\text{O}_4$ .<sup>35</sup> Moreover, the high-resolution O 1s spectrum is fit into two peaks located at 530.32 eV and 531.97 eV, corresponding to the -C=O and -C-OH, respectively (**Figure 2f**).<sup>36</sup> These results confirmed the formation of  $\text{Co}_3\text{O}_4$  from the above processes.

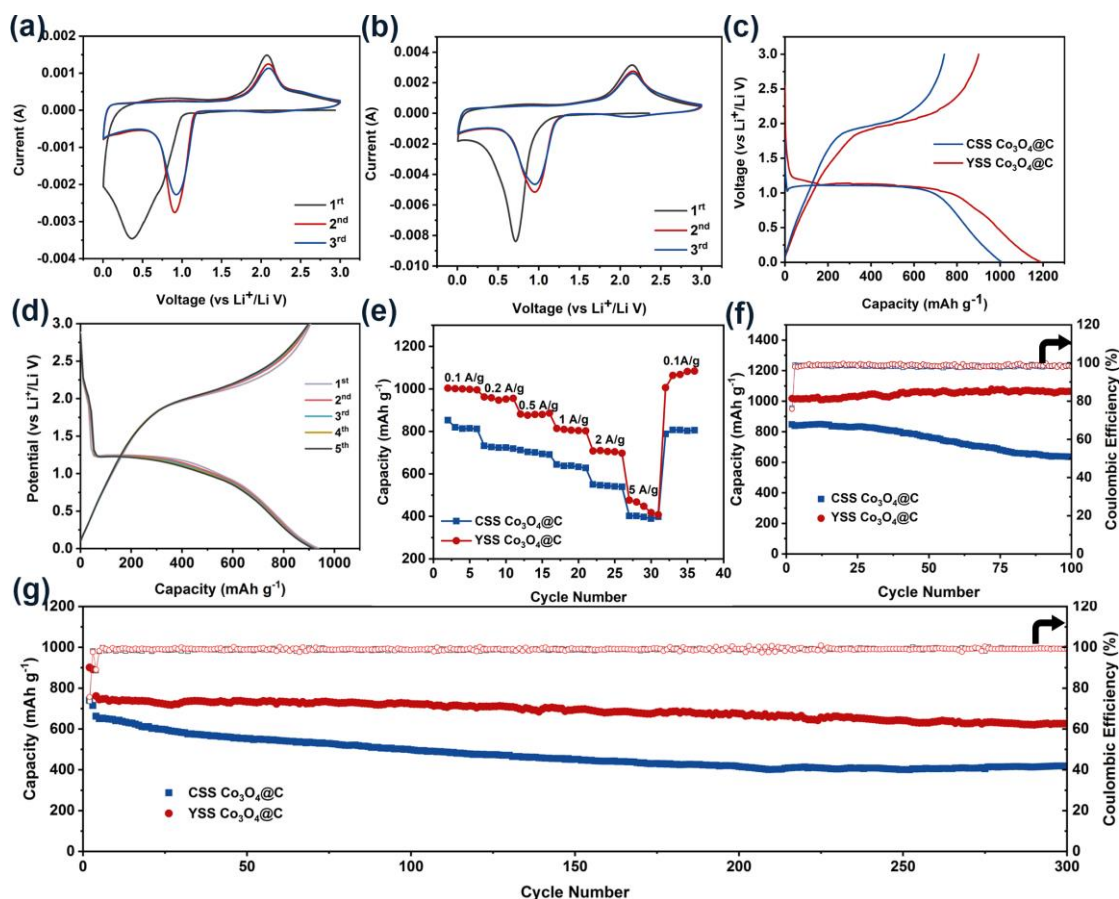


**Figure 3.** (a, b) Cyclic voltammetry (CV) curves at a scan rate of 0.5 mV s<sup>-1</sup>; (c) The first charge/discharge at a current density of 0.1 A g<sup>-1</sup> of CSS

Co<sub>3</sub>O<sub>4</sub>@C and YSS Co<sub>3</sub>O<sub>4</sub>@C. (d) The first five discharge and charge voltage profiles at 0.5 A g<sup>-1</sup> of YSS Co<sub>3</sub>O<sub>4</sub>@C. (e) The rate performance at various current densities and (f, g) long-term performance at the current density of 0.1 A g<sup>-1</sup> and 1 A g<sup>-1</sup> for the CSS Co<sub>3</sub>O<sub>4</sub>@C and YSS Co<sub>3</sub>O<sub>4</sub>@C.

In the light of high Co<sub>3</sub>O<sub>4</sub> content and yolk-shell structure, the CSS Co<sub>3</sub>O<sub>4</sub>@C and YSS Co<sub>3</sub>O<sub>4</sub>@C nanoparticles were used as the anode materials for the LIBs. The initial three cycles of the CV curves of CSS Co<sub>3</sub>O<sub>4</sub>@C and YSS Co<sub>3</sub>O<sub>4</sub>@C nanoparticles at a scan rate of 0.5 mV s<sup>-1</sup> are displayed in **Figure 3a** and **3b**, respectively. For the first cathodic scan, a strong and sharp peak is observed at 0.75 V, corresponding to the reduction of the Co<sub>3</sub>O<sub>4</sub> and the formation of the solid-electrolyte interphase layer (SEI).<sup>37</sup> In the following scan cycles, this peak shifts to the higher voltage and became weaker due to the activation process and stable SEI film. The peak at ~ 2.1 V in the anodic scan is a result of oxidation of Co into Co<sub>3</sub>O<sub>4</sub>.<sup>38</sup> The CV curves almost overlap in the subsequent cycles, indicating superior reversibility and good cycling stability during the charge/discharge processes.<sup>39</sup> **Figure 3c** shows the first galvanostatic charge-discharge profiles of the CSS Co<sub>3</sub>O<sub>4</sub>@C and the YSS Co<sub>3</sub>O<sub>4</sub>@C nanoparticles in the voltage window of 0.005-3.0 V at a current density of 0.1 A g<sup>-1</sup>. A voltage platform with a slow decline at about 1.05-1.25 V is observed, which is consistent with previous reports.<sup>40</sup> The initial specific charge/discharge capacity is 1190/901 mAh g<sup>-1</sup> for the YSS Co<sub>3</sub>O<sub>4</sub>@C nanoparticles with a

Columbic efficiency of 75.7%, and were 1008/741 mAh g<sup>-1</sup> for the CSS Co<sub>3</sub>O<sub>4</sub>@C nanoparticles with a Columbic efficiency of 73.5%. The irreversible capacity loss can be attributed to the formation of the SEI layer.<sup>41</sup> **Figure 3d** exhibits galvanostatic charge/discharge (GCD) curves of YSS Co<sub>3</sub>O<sub>4</sub>@C nanoparticles anode at 0.5 A g<sup>-1</sup> for the first five cycles. The overlapped curves suggest high reversibility of electrochemical reaction, which is further confirmed by the CV curves.

The rate performance of the electrode including CSS Co<sub>3</sub>O<sub>4</sub>@C and YSS Co<sub>3</sub>O<sub>4</sub>@C nanoparticles was further investigated by increasing the current density from 0.1 A g<sup>-1</sup> to 5 A g<sup>-1</sup> and then returning to 0.1 A g<sup>-1</sup>. The reversible capacity falls moderately with an increase of the current density. **Figure 3e** shows that reversible capacity of the YSS Co<sub>3</sub>O<sub>4</sub>@C nanoparticles is higher than that of the CSS Co<sub>3</sub>O<sub>4</sub>@C nanoparticles, possibly due to the stress release during the charge/discharge process because of the presence of the void space. Interestingly, the percent of capacity retain is 106% for the YSS Co<sub>3</sub>O<sub>4</sub>@C as the current density decreased back to 0.1 A g<sup>-1</sup>, which is characteristic profile in the cobalt-based electrode materials.<sup>42-43</sup> This phenomenon can be explained by the activation process that enabled to improvement Li<sup>+</sup> diffusion kinetics, which created a considerable accessibility for Li<sup>+</sup> insertion/extraction from the anode materials.<sup>21</sup> It is quite clear that YSS Co<sub>3</sub>O<sub>4</sub>@C nanoparticles show a superior performance that can be demonstrated by the presence of the void space that can prevent the

aggregation of  $\text{Co}_3\text{O}_4$  nanoparticles and facile charge transport occur with remarkable kinetic feature under high rates.<sup>44</sup>

The long-term electrochemical performance at current densities  $0.1 \text{ A g}^{-1}$  and  $1 \text{ A g}^{-1}$  was investigated to further understand cycle stability of these electrode materials, as shown in **Figure 3f** and **3g**. The YSS  $\text{Co}_3\text{O}_4@\text{C}$  nanoparticles electrode delivered high initial reversible capacity of  $1016 \text{ mAh g}^{-1}$  at  $0.1 \text{ A g}^{-1}$ , and still remain a large reversible capacity of  $1066 \text{ mAh g}^{-1}$  even after 100 cycles (seen in **Figure 3f**). In contrast, gradual capacity decay can be observed in the CSS  $\text{Co}_3\text{O}_4@\text{C}$  nanoparticles with the first reversible capacity of  $848 \text{ mAh g}^{-1}$  and final capacity of  $630 \text{ mAh g}^{-1}$  after 100 charge/discharge cycles. As the current density increased to  $1 \text{ A g}^{-1}$ , the YSS  $\text{Co}_3\text{O}_4@\text{C}$  nanoparticles electrode showed excellent capacity retention during the charge/discharge cycles. The reversible capacity ( $626 \text{ mAh g}^{-1}$ ) was much higher than that of the CSS  $\text{Co}_3\text{O}_4@\text{C}$  nanoparticles ( $419 \text{ mAh g}^{-1}$ ) after 300 charge/discharge cycles, indicating that the YSS  $\text{Co}_3\text{O}_4@\text{C}$  nanoparticles shows higher stability than the CSS  $\text{Co}_3\text{O}_4@\text{C}$  nanoparticles. The YSS  $\text{Co}_3\text{O}_4@\text{C}$  electrode shows a much higher specific capacity than other  $\text{Co}_3\text{O}_4$ -carbon based electrode materials in the literature (**Table S2**). Meanwhile, the morphology and inner structure of the electrodes were observed after long-term cycling, as shown in **Figure S7**. It is essential to note the YSS  $\text{Co}_3\text{O}_4@\text{C}$  nanoparticles still remain the original yolk-shell structure after 300 cycles.

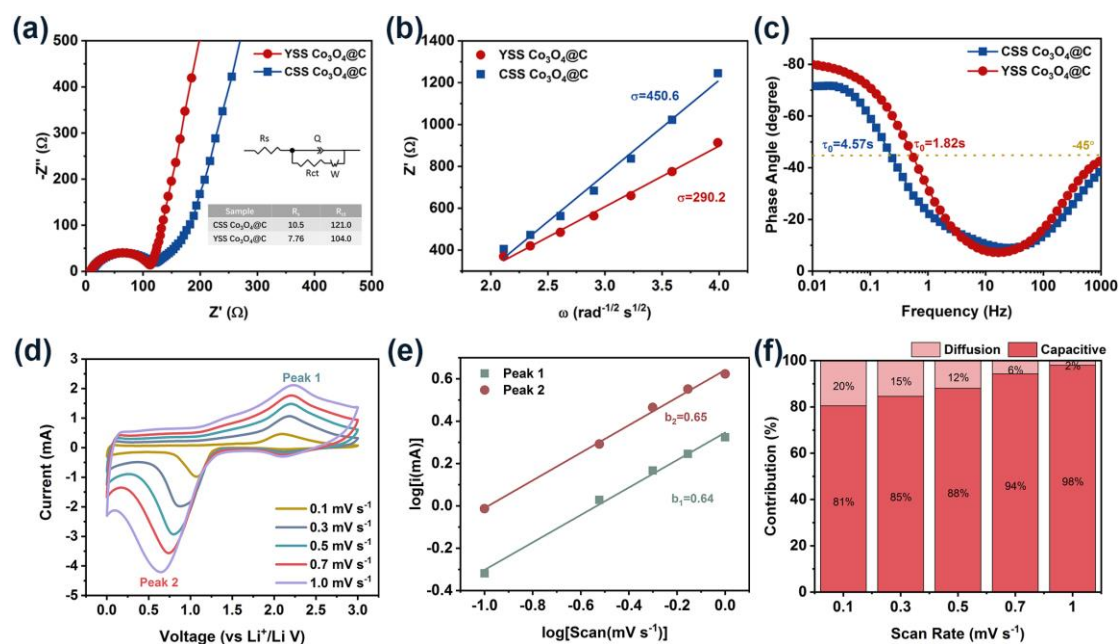


**Figure 4.** (a) Nyquist plots (inset: a fitting equivalent circuit model and corresponding fitting values); (b) Relationship between  $Z'$  and  $\omega^{-1/2}$  ( $\omega = 2\pi f$ ); (c) Bode plots of CSS  $\text{Co}_3\text{O}_4$ @C and YSS  $\text{Co}_3\text{O}_4$ @C nanoparticles. (d) CV curves at various scan rates; (e)  $\log(i)$  versus  $\log(v)$  plots at different cathodic/anodic peaks and (f) contribution ratios of pseudocapacitive controlled (dark red) and diffusion-controlled capacities (light red) at scan rates from 0.1  $\text{mV s}^{-1}$  to 1.0  $\text{mV s}^{-1}$  of YSS  $\text{Co}_3\text{O}_4$ @C nanoparticles.

The EIS was employed to clarify the charge transfer reaction kinetics of CSS  $\text{Co}_3\text{O}_4$ @C and YSS  $\text{Co}_3\text{O}_4$ @C nanoparticles, respectively. The Nyquist plots and the corresponding equivalent circuit model are shown in **Figure 4a**, in which  $R_s$  corresponds to the bulk series resistance of the electrode, the semicircle in the high frequency region represents the charge transfer resistance ( $R_{ct}$ ), and the slope of the straight line at the low frequency region stands for the Warburg impedance.<sup>38, 45</sup> It is clear observed that the decreased

semicircle and the increased slope for the YSS Co<sub>3</sub>O<sub>4</sub>@C nanoparticles than for the CSS Co<sub>3</sub>O<sub>4</sub>@C nanoparticles. The YSS Co<sub>3</sub>O<sub>4</sub>@C and CSS Co<sub>3</sub>O<sub>4</sub>@C showed  $R_{ct}$  of 104  $\Omega$  and 121  $\Omega$ , respectively (**Figure 4a**, inset). Consequently, the YSS Co<sub>3</sub>O<sub>4</sub>@C electrode shows an effective faradaic reaction at the boundary of the electrode and electrolyte due to the presence of the void space, which resulted in higher electrochemical performance <sup>46</sup>. Moreover, the Li<sup>+</sup> diffusion coefficient ( $D$ ) can be determined according to the **Eqs.(1) and (2)**. The Warburg impedance coefficient ( $\sigma$ ) can be obtained by fitting the straight line between  $Z'$  and  $\omega^{-1/2}$  in the low-frequency region <sup>47</sup>. Based on the results shown in **Figure 4b**, the YSS Co<sub>3</sub>O<sub>4</sub>@C nanoparticles exhibit higher diffusion coefficient ( $\sigma = 290.2$ ) as compared to the CSS Co<sub>3</sub>O<sub>4</sub>@C ( $\sigma = 450.6$ ), indicating structural stability due to the presence of the void space in the YSS Co<sub>3</sub>O<sub>4</sub>@C nanoparticles, which results in improved diffusion of the lithium ions and facilitated volume expansion during the repeated lithiation/delithiation cycles <sup>48</sup>. Moreover, as shown in the Bode plot (**Figure 4c**), the phase angle of YSS Co<sub>3</sub>O<sub>4</sub>@C nanoparticles is close to -90° at 0.01 Hz, and whereas and CSS Co<sub>3</sub>O<sub>4</sub>@C electrode exhibits a sluggish frequency response with a phase angle of -70° at 0.01 Hz. The relaxation time constant  $\tau_0$  ( $\tau_0 = 1/f_0$ ,  $f_0$  is the characteristic frequency at -45°) is 1.82s for YSS Co<sub>3</sub>O<sub>4</sub>@C, which is lower than that of CSS Co<sub>3</sub>O<sub>4</sub>@C ( $\tau_0 = 4.57$ s), confirming a fast ion transport inner the void space. <sup>49</sup>

To further explore the superior electrochemical performance of YSS

Co<sub>3</sub>O<sub>4</sub>@C nanoparticles abide for the LIBs, the reaction kinetics was studied by CV measurements under various scan rates from 0.1 mV s<sup>-1</sup> to 1.0 mV s<sup>-1</sup>. Considering the existence of the polarization, the peak current is chosen rather than the same voltage in each cycle. As presented in **Figure 4d**, the relationship between scan rate ( $v$ ) and current ( $i$ ) can be expressed as follows: <sup>50</sup>

$$i = av^b \quad (3)$$

$$\log(i) = b \log(v) + \log(a) \quad (4)$$

where  $a$  and  $b$  are constants. Commonly, the electrochemical behavior is controlled by the ionic diffusion process when the  $b$ -value is 0.5, and pseudocapacitive-controlled Li<sup>+</sup> storage if the  $b=1.0$ , which corresponds to capacitive and battery behavior.<sup>13</sup> In **Figure 4e**, the fitted  $b$  values according to cathodic and anodic peaks are 0.64 and 0.65, suggesting the electro-reaction is influenced by the diffusion-controlled and pseudocapacitive controlled process.<sup>51</sup> Furthermore, the contribution from pseudo-capacitive on the total charge storage is quantified based on the following equation:<sup>38</sup>

$$i = k_1v + k_2v^{1/2} \quad (5)$$

where  $k_1v$  presents the pseudo-capacitance and  $k_2v^{1/2}$  describes the diffusion-controlled contribution. By determining  $k_1$  and  $k_1$  at a fixed voltage, the contribution ratios of pseudo-capacitance and diffusion-controlled can be obtained. As shown in **Figure 4f**, the contribution ratio (dark red area) of pseudo-capacitance behavior to the total charge is 81% at a scan rate of 0.1 mV s<sup>-1</sup>. The ratios of pseudo-capacitance contribution rise from 85% to 98%

as the sweep rate increase from  $0.3 \text{ mV s}^{-1}$  to  $1.0 \text{ mV s}^{-1}$ , indicating the electrochemical process was dominant controlled by this kind of charge storage behavior.<sup>17, 52</sup>

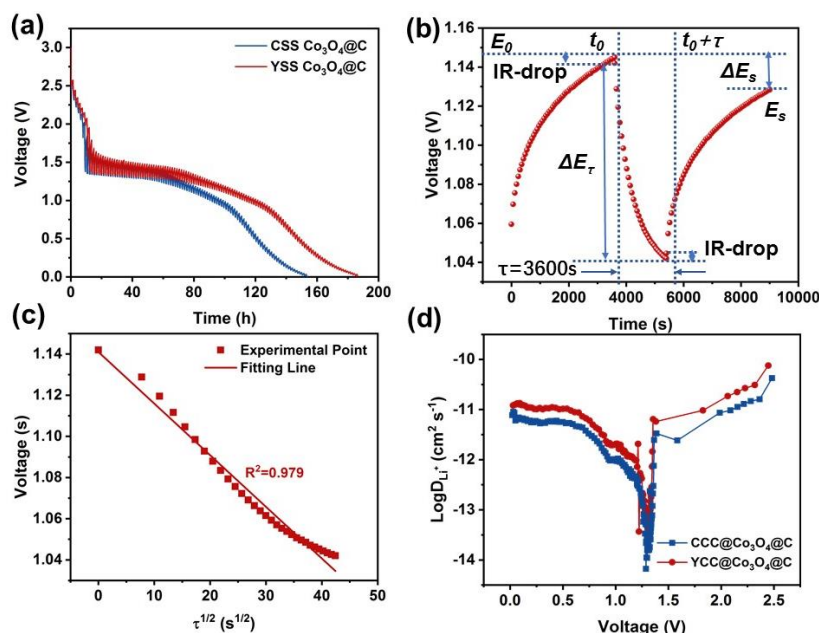


**Figure. 5.** (a) GITT curves of the CSS Co<sub>3</sub>O<sub>4</sub>@C and YSS Co<sub>3</sub>O<sub>4</sub>@C nanoparticles at discharge state. (b) Time vs.  $E$  profile for a single GITT titration; (c) fitting line between the  $E$  vs.  $\tau^{1/2}$  of YSS Co<sub>3</sub>O<sub>4</sub>@C. (d) Li<sup>+</sup> diffusion coefficients at different charge states of CSS Co<sub>3</sub>O<sub>4</sub>@C and YSS Co<sub>3</sub>O<sub>4</sub>@C.

To explicate the enhanced electrochemical performance of YSS Co<sub>3</sub>O<sub>4</sub>@C nanoparticles electrode, the diffusing kinetics of the lithium ion were investigated by the galvanostatic intermittent titration technique (GITT), as shown in **Fig. 5**. The GITT curves of CSS Co<sub>3</sub>O<sub>4</sub>@C and YSS Co<sub>3</sub>O<sub>4</sub>@C electrode as a function of time in the voltage window from 0.005-3.0V, in **Fig.5a**. The measurements were employed on the second cycle with an interval of 30 min discharge/charge and a long time interval of 1 hour at a small current

density of 20 mA g<sup>-1</sup>. The plateaus of the discharge/charge in the GITT plots are consistent with the normal charge and discharge curves. Furthermore, the YSS Co<sub>3</sub>O<sub>4</sub>@C showed a longer test time than that of CSS Co<sub>3</sub>O<sub>4</sub>@C suggests the higher discharge capacitance, which is also consistent with the GCD results. The chemical diffusion coefficient of Li<sup>+</sup> was calculated based on formula follow<sup>53</sup>

$$D = \frac{4}{\pi} \left( \frac{mV_M}{MS} \right)^2 \left( \frac{dE/dx}{dE/d\tau^{1/2}} \right)^2 (\tau \ll L^2/D_{Li}) \quad (6)$$

in where  $m$  and  $M$  indicated the molecular weight and mass of electrode,  $V_m$  represented the molar volume of the materials,  $S$  means the surface area of the electrode. **Fig. 5b** presented the voltage response of the YSS Co<sub>3</sub>O<sub>4</sub>@C nanoparticles electrode during a single step of titration and the corresponding parameters were illustrated. If the voltage ( $E$ ) showed a good linear correlation with the interruption time ( $\tau^{1/2}$ ) over the entire period of current flux, **Eq. (6)** can be simplified as **Eq. (7)**, as shown in **Fig. 5c**.

$$D = \frac{4}{\pi\tau} \left( \frac{mV_M}{MS} \right)^2 \left( \frac{\Delta E_S}{\Delta E_\tau} \right)^2 \quad (7)$$

where  $\tau$  is the applied current pulse time,  $\Delta E_S$  is the total charge of voltage during the current pulse and  $\Delta E_\tau$  expressed steady-state potential variation during the galvanostatic titration.

The diffusion coefficients Li<sup>+</sup> can be obtained based on the **Eq. 7** and GITT measurements, as presented in **Fig. 5d**. The Li<sup>+</sup> diffusion coefficients ( $D_{Li^+}$ ) of YSS Co<sub>3</sub>O<sub>4</sub>@C electrode ( $2.08 \times 10^{-14}$  to  $7.54 \times 10^{-11}$  cm<sup>2</sup> s<sup>-1</sup>) are larger than those of CSS Co<sub>3</sub>O<sub>4</sub>@C electrode ( $6.67 \times 10^{-15}$  to  $4.23 \times 10^{-11}$  cm<sup>2</sup> s<sup>-1</sup>) during

the whole lithiation/delithiation processes. The minimum  $D_{Li^+}$  was obtained at around the platform voltage during the discharge procedure, which derived from the phase transition of  $\text{Co}_3\text{O}_4$  in the lithium-ion insertion/extraction processes.<sup>54</sup> Besides, the  $\text{N}_2$  isotherms were employed to estimate the specific surface area, as shown in **Figure S8a**. The specific surface area of YSS  $\text{Co}_3\text{O}_4@\text{C}$  was calculated to be  $191.2 \text{ m}^2\text{g}^{-1}$  based on the DFT method, which is higher than that of CSS  $\text{Co}_3\text{O}_4@\text{C}$  ( $127.8 \text{ m}^2\text{g}^{-1}$ )<sup>55</sup>. The pore size distribution further proves that YSS  $\text{Co}_3\text{O}_4@\text{C}$  exhibited a larger pore size. (**Figure S8b**). The large specific surface area will increase the contact area between the electrode and electrolyte, leading to fast electrochemical kinetics and improved performance<sup>56</sup>.

Based on the above analysis, it is confirmed that plastic waste derived YSS  $\text{Co}_3\text{O}_4@\text{C}$  nanoparticles show much improved electrochemical performance than that of CSS  $\text{Co}_3\text{O}_4@\text{C}$  nanoparticles in lithium-ion batteries. It is further demonstrated that the plastic waste can be well recycled and upgraded to the high-value-added product.

## Conclusions

In summary, we report a highly efficient and effective approach to converting plastic wastes (waste mask, waste plastic jar and foam sheets) into YSS  $\text{Co}_3\text{O}_4@\text{C}$  nanoparticles in large scale. The obtained plastic waste derived YSS  $\text{Co}_3\text{O}_4@\text{C}$  electrode shows a high electrochemical performance when used as the anode material for LIBs, with an initial discharge capacity of  $1190 \text{ mAh g}^{-1}$  a Columbic efficiency of 75.7%. Cycling tests showed that

stable cycling ability of 1066 mAh g<sup>-1</sup> at a current density of 0.1 A g<sup>-1</sup> after 100 charge/discharge cycles, and excellent cycle performance. The void space in the YSS Co<sub>3</sub>O<sub>4</sub>@C nanoparticles decreased the Li<sup>+</sup> ion diffusion pathway and released the stress generated by the volume increase during Li<sup>+</sup> ion transportation into the electrode materials, leading to an excellent electrochemical performance. The galvanostatic intermittent titration technique (GITT) results proved the above results. This work provides a facile way for the design of high-performance anode materials of LIBs by recycling of the plastic wastes.

## **ASSOCIATED CONTENT**

### **Supporting Information**

The yield of single component waste polymer (PP, PE or PS) and Co<sub>3</sub>O<sub>4</sub> after carbonization, the mechanism about the conversion of mixed plastics (PP, PE and PS) into YSS Co<sub>3</sub>O<sub>4</sub>@C. SEM image, EDX mapping images and XRD curve of Sphere Co<sub>3</sub>O<sub>4</sub>. SEM and EDX mapping images of P-Co<sub>3</sub>O<sub>4</sub> composites, CSS Co@C. TGA curves of YSS Co<sub>3</sub>O<sub>4</sub>@C. Comparison of the performance of the Co<sub>3</sub>O<sub>4</sub> based LIB electrode materials. SEM and TEM images after 300 cycles at 1 A g<sup>-1</sup> of CSS Co<sub>3</sub>O<sub>4</sub>@C and YSS Co<sub>3</sub>O<sub>4</sub>@C. N<sub>2</sub> isotherms and corresponding PSD curves of CSS Co<sub>3</sub>O<sub>4</sub>@C and YSS Co<sub>3</sub>O<sub>4</sub>@C.

## **AUTHOR INFORMATION**

Corresponding authors:

**Xuecheng Chen** - Faculty of Chemical Technology and Engineering, West Pomeranian University of Technology, Szczecin, Piastów Ave. 42, Szczecin 71-065, Poland.

*E-mail:* xchen@zut.edu.pl (X. Chen)

**Dengsong Zhang** - School of Materials Science and Engineering & Research Center of Nano Science and Technology, Shanghai University, Shanghai 200444, China.

*E-mail:* dszhang@shu.edu.cn (D. Zhang)

Authors:

**Jiaxin Li** - Faculty of Chemical Technology and Engineering, West Pomeranian University of Technology, Szczecin, Piastów Ave. 42, Szczecin 71-065, Poland.

**Fei Dou** - School of Materials Science and Engineering & Research Center of Nano Science and Technology, Shanghai University, Shanghai 200444, China.

**Jiang Gong** - Key Laboratory of Material Chemistry for Energy Conversion and Storage, Ministry of Education, School of Chemistry and Chemical Engineering, Huazhong University of Science and Technology, Wuhan 430074, China.

**Yumeng Hua:** - School of Environment and Chemical Engineering, Shenyang University of Technology, Shenyang 110870, China

**Yanshen Gao:** - Faculty of Chemical Technology and Engineering, West Pomeranian University of Technology, Szczecin, Piastów Ave. 42, Szczecin 71-065, Poland.

**Krzysztof Sielicki** - Faculty of Chemical Technology and Engineering, West Pomeranian University of Technology, Szczecin, Piastów Ave. 42, Szczecin 71-065, Poland.

**Ewa Mijowska** - Faculty of Chemical Technology and Engineering, West Pomeranian University of Technology, Szczecin, Piastów Ave. 42, Szczecin 71-065, Poland.

§J. L. and F. D contributed equally to this paper.

### **Author Contributions**

X. C., and D. Z. designed the project; J. L., and F. D. completed the experiments and electrochemical test; J. G. co-wrote manuscript; Y. H and Y. G. completed the GITT; GK. S. analyzed the data and provide TEM measurement. E. M. revised the manuscript. All the authors contributed the manuscript.

### **Notes**

The authors declare no competing financial interest.

### **ACKNOWLEDGMENT**

The authors are grateful for the financial support from the National Science Centre (NCN), Poland, UMO-2020/39/B/ST8/02937.

### **References**

- (1) Amobonye, A.; Bhagwat, P.; Singh, S.; Pillai, S. Plastic biodegradation: Frontline microbes and their enzymes. *Sci Total Environ* **2021**, *759*, 143536, DOI: 10.1016/j.scitotenv.2020.143536.
- (2) Gong, J.; Chen, X.; Tang, T. Recent progress in controlled carbonization of (waste) polymers. *Progress in Polymer Science* **2019**, *94*, 1-32, DOI: 10.1016/j.progpolymsci.2019.04.001.
- (3) Jung, S.; Lee, S.; Dou, X.; Kwon, E. E. Valorization of disposable COVID-19 mask through the thermo-chemical process. *Chem Eng J* **2021**, *405*, 126658, DOI: 10.1016/j.cej.2020.126658.

- (4) Chen, J.; Wu, J.; Sherrell, P. C.; Chen, J.; Wang, H.; Zhang, W. X.; Yang, J. How to build a microplastics-free environment: strategies for microplastics degradation and plastics recycling. *Adv Sci (Weinh)* **2022**, *9* (6), 2103764, DOI: 10.1002/advs.202103764.
- (5) Panahi, A.; Sun, X.; Song, G.; Levendis, Y. A. On the influences of carrier gas type and flow rate on cvd synthesis of cnts from postconsumer polyethylene. *Ind Eng Chem Res* **2020**, *59* (31), 14004-14014, DOI: 10.1021/acs.iecr.0c02000.
- (6) Khalid, M. Y.; Arif, Z. U.; Ahmed, W.; Arshad, H. Recent trends in recycling and reusing techniques of different plastic polymers and their composite materials. *Sustainable Materials and Technologies* **2022**, *31*, e00382, DOI: 10.1016/j.susmat.2021.e00382.
- (7) Sun, L.; Deng, Q.; Li, Y.; Mi, H.; Wang, S.; Deng, L.; Ren, X.; Zhang, P. CoO-Co<sub>3</sub>O<sub>4</sub> heterostructure nanoribbon/RGO sandwich-like composites as anode materials for high performance lithium-ion batteries. *Electrochim Acta* **2017**, *241*, 252-260, DOI: 10.1016/j.electacta.2017.04.148.
- (8) Gong, J.; Liu, J.; Chen, X.; Jiang, Z.; Wen, X.; Mijowska, E.; Tang, T. One-pot synthesis of core/shell Co@C spheres by catalytic carbonization of mixed plastics and their application in the photo-degradation of Congo red. *J. Mater. Chem. A* **2014**, *2* (20), 7461-7470, DOI: 10.1039/c4ta00173g.
- (9) Jeswani, H.; Kruger, C.; Russ, M.; Horlacher, M.; Antony, F.; Hann, S.; Azapagic, A. Life cycle environmental impacts of chemical recycling via pyrolysis of mixed plastic waste in comparison with mechanical recycling and energy recovery. *Sci Total Environ* **2021**, *769*, 144483, DOI: 10.1016/j.scitotenv.2020.144483.
- (10) Veksha, A.; Yin, K.; Moo, J. G. S.; Oh, W. D.; Ahamed, A.; Chen, W. Q.; Weerachanchai, P.; Giannis, A.; Lisak, G. Processing of flexible plastic packaging waste into pyrolysis oil and multi-walled carbon nanotubes for electrocatalytic oxygen reduction. *J Hazard Mater* **2020**, *387*, 121256, DOI: 10.1016/j.jhazmat.2019.121256.
- (11) Jing, Y.; Wang, Y.; Furukawa, S.; Xia, J.; Sun, C.; Hulseley, M. J.; Wang, H.; Guo, Y.; Liu, X.; Yan, N. Towards the circular economy: converting aromatic plastic waste back to arenes over a Ru/Nb<sub>2</sub>O<sub>5</sub> catalyst. *Angew Chem Int Ed Engl* **2021**, *60* (10), 5527-5535, DOI: 10.1002/anie.202011063.
- (12) Kunwar, B.; Cheng, H. N.; Chandrashekar, S. R.; Sharma, B. K. Plastics to fuel: a review. *Renewable and Sustainable Energy Reviews* **2016**, *54*, 421-428, DOI: 10.1016/j.rser.2015.10.015.
- (13) Huang, S.; Yang, L.; Xu, G.; Wei, T.; Tian, J.; Liu, X.; Li, H.; Xiang, Z.; Cao, J.; Wei, X. Hollow Co<sub>3</sub>O<sub>4</sub>@N-doped carbon nanocrystals anchored on carbon nanotubes for freestanding anode with superior Li/Na storage performance. *Chem Eng J* **2021**, *415*, 128861, DOI: 10.1016/j.cej.2021.128861.
- (14) Chen, H.; Xia, W.; Wang, S. Biodiesel production from waste cooking oil using a waste diaper derived heterogeneous magnetic catalyst. *Brazilian Journal of Chemical Engineering* **2022**, DOI: 10.1007/s43153-022-00257-z.
- (15) Idrees, M.; Batool, S.; Kong, J.; Zhuang, Q.; Liu, H.; Shao, Q.; Lu, N.; Feng, Y.; Wujcik, E. K.; Gao, Q.; Ding, T.; Wei, R.; Guo, Z. Polyborosilazane derived ceramics - Nitrogen sulfur dual doped graphene nanocomposite anode for enhanced lithium ion batteries. *Electrochim Acta* **2019**, *296*, 925-937, DOI: 10.1016/j.electacta.2018.11.088.
- (16) Yang, Q.; Feng, C.; Liu, J.; Guo, Z. Synthesis of porous Co<sub>3</sub>O<sub>4</sub>/C nanoparticles as anode for Li-ion battery application. *Appl Surf Sci* **2018**, *443*, 401-406, DOI: 10.1016/j.apsusc.2018.02.230.
- (17) Cong, L.; Zhang, S.; Zhu, H.; Chen, W.; Huang, X.; Xing, Y.; Xia, J.; Yang, P.; Lu, X. Structure-design and theoretical-calculation for ultras-small Co<sub>3</sub>O<sub>4</sub> anchored into ionic liquid modified graphene as anode of flexible lithium-ion batteries. *Nano Research* **2021**, *15* (3), 2104-2111, DOI: 10.1007/s12274-021-3836-7.

- (18) Xue, H.; Na, Z.; Wu, Y.; Wang, X.; Li, Q.; Liang, F.; Yin, D.; Wang, L.; Ming, J. Unique Co<sub>3</sub>O<sub>4</sub>/nitrogen-doped carbon nanospheres derived from metal–organic framework: insight into their superior lithium storage capabilities and electrochemical features in high-voltage batteries. *J Mater Chem A* **2018**, *6* (26), 12466-12474, DOI: 10.1039/c8ta03959c.
- (19) Kim, S.; Lim, Y.; Kang, T.-H.; Moon, J.; Choi, I.-S.; Lee, Y. J.; Yi, H. Biotemplated nanocomposites of transition-metal oxides/carbon nanotubes with highly stable and efficient electrochemical interfaces for high-power lithium-ion batteries. *ACS Applied Energy Materials* **2020**, *3* (8), 7804-7812, DOI: 10.1021/acsaem.0c01208.
- (20) Gu, F.; Liu, W.; Huang, R.; Song, Y.; Jia, J.; Wang, L. A g-C<sub>3</sub>N<sub>4</sub> self-templated preparation of N-doped carbon nanosheets@Co-Co<sub>3</sub>O<sub>4</sub>/Carbon nanotubes as high-rate lithium-ion batteries' anode materials. *J Colloid Interface Sci* **2021**, *597*, 1-8, DOI: 10.1016/j.jcis.2021.03.163.
- (21) Zhao, Y.; Liu, C.; Yi, R.; Li, Z.; Chen, Y.; Li, Y.; Mitrovic, I.; Taylor, S.; Chalker, P.; Yang, L.; Zhao, C. Facile preparation of Co<sub>3</sub>O<sub>4</sub> nanoparticles incorporating with highly conductive MXene nanosheets as high-performance anodes for lithium-ion batteries. *Electrochim Acta* **2020**, *345*, 136203, DOI: 10.1016/j.electacta.2020.136203.
- (22) Huang, M.-X.; Sun, Y.-H.; Guan, D.-C.; Nan, J.-M.; Cai, Y.-P. Hydrothermal synthesis of mesoporous SnO<sub>2</sub> as a stabilized anode material of lithium-ion batteries. *Ionics* **2019**, *25* (12), 5745-5757, DOI: 10.1007/s11581-019-03127-w.
- (23) Gao, S.; Wang, N.; Li, S.; Li, D.; Cui, Z.; Yue, G.; Liu, J.; Zhao, X.; Jiang, L.; Zhao, Y. Multi-wall Sn/SnO<sub>2</sub>@carbon hollow nanofibers anode material for high-rate and long-life lithium-ion batteries. *Angew Chem Int Ed Engl* **2019**, *59*, 2465–2472, DOI: 10.1002/anie.201913170.
- (24) Gong, J.; Liu, J.; Jiang, Z.; Chen, X.; Wen, X.; Mijowska, E.; Tang, T. Converting mixed plastics into mesoporous hollow carbon spheres with controllable diameter. *Applied Catalysis B: Environmental* **2014**, *152-153*, 289-299, DOI: 10.1016/j.apcatb.2014.01.051.
- (25) Wang, J.; Wang, H.; Yao, T.; Liu, T.; Tian, Y.; Li, C.; Li, F.; Meng, L.; Cheng, Y. Porous N-doped carbon nanoflakes supported hybridized SnO<sub>2</sub>/Co<sub>3</sub>O<sub>4</sub> nanocomposites as high-performance anode for lithium-ion batteries. *J Colloid Interface Sci* **2020**, *560*, 546-554, DOI: 10.1016/j.jcis.2019.10.096.
- (26) Zhong, M.; He, W. W.; Shuang, W.; Liu, Y. Y.; Hu, T. L.; Bu, X. H. Metal-organic framework derived core-shell Co/Co<sub>3</sub>O<sub>4</sub>@N-C nanocomposites as high performance anode materials for lithium ion batteries. *Inorg Chem* **2018**, *57* (8), 4620-4628, DOI: 10.1021/acs.inorgchem.8b00365.
- (27) Wen, Y.; Kierzek, K.; Min, J.; Chen, X.; Gong, J.; Niu, R.; Wen, X.; Azadmanjiri, J.; Mijowska, E.; Tang, T. Porous carbon nanosheet with high surface area derived from waste poly(ethylene terephthalate) for supercapacitor applications. *Journal of Applied Polymer Science* **2019**, *137* (5), 48338, DOI: 10.1002/app.48338.
- (28) Liu, X.; Ma, C.; Wen, Y.; Chen, X.; Zhao, X.; Tang, T.; Holze, R.; Mijowska, E. Highly efficient conversion of waste plastic into thin carbon nanosheets for superior capacitive energy storage. *Carbon* **2021**, *171*, 819-828, DOI: 10.1016/j.carbon.2020.09.057.
- (29) Zhou, C.; Wang, D.; Li, A.; Pan, E.; Liu, H.; Chen, X.; Jia, M.; Song, H. Three-dimensional porous carbon doped with N, O and P heteroatoms as high-performance anode materials for sodium ion batteries. *Chem Eng J* **2020**, *380*, (15), 122457, DOI: 10.1016/j.cej.2019.122457.
- (30) Hulicova-Jurcakova, D.; Seredych, M.; Lu, G. Q.; Bandoz, T. J. Combined effect of nitrogen- and oxygen-containing functional groups of microporous activated carbon on its electrochemical performance in supercapacitors. *Adv Funct Mater* **2009**, *19* (3), 438-447, DOI: 10.1002/adfm.200801236.

- (31) Li, J. X.; Michalkiewicz, B.; Min, J. K.; Ma, C. D.; Chen, X. C.; Gong, J.; Mijowska, E.; Tang, T. Selective preparation of biomass-derived porous carbon with controllable pore sizes toward highly efficient CO<sub>2</sub> capture. *Chem Eng J* **2019**, *360*, 250-259, DOI: 10.1016/j.cej.2018.11.204.
- (32) Zhu, J.; Tu, W.; Pan, H.; Zhang, H.; Liu, B.; Cheng, Y.; Deng, Z.; Zhang, H. Self-templating synthesis of hollow Co<sub>3</sub>O<sub>4</sub> nanoparticles embedded in n,s-dual-doped reduced graphene oxide for lithium ion batteries. *ACS Nano* **2020**, *14* (5), 5780-5787, DOI: 10.1021/acsnano.0c00712.
- (33) Choudhury, B. J.; Muigai, H. H.; Kalita, P.; Moholkar, V. S. Biomass blend derived porous carbon for aqueous supercapacitors with commercial-level mass loadings and enhanced energy density in redox-active electrolyte. *Appl Surf Sci* **2022**, *601*, 154202, DOI: 10.1016/j.apsusc.2022.154202.
- (34) Lu, X.; Liu, A.; Zhang, Y.; Liu, S. Space-confined synthesis of yolk-shell structured Co<sub>3</sub>O<sub>4</sub>/nitrogen-doped carbon nanocomposites with hollow mesoporous carbon nanocages as advanced functional anodes for lithium-ion batteries. *ACS Applied Energy Materials* **2020**, *3* (11), 11153-11163, DOI: 10.1021/acsaem.0c02098.
- (35) Wang, J.; Wang, C.; Zhen, M. Template-free synthesis of multifunctional Co<sub>3</sub>O<sub>4</sub> nanotubes as excellent performance electrode materials for superior energy storage. *Chem Eng J* **2019**, *356*, 1-10, DOI: 10.1016/j.cej.2018.09.014.
- (36) Li, J.; Chen, X.; Gong, J.; Zhu, J.; Mijowska, E. Deep insight into the pore size distribution of N-doped porous carbon materials on electrochemical energy storage and CO<sub>2</sub> sorption. *Diamond and Related Materials* **2020**, *105*, 107802, DOI: 10.1016/j.diamond.2020.107802.
- (37) Sun, B.; Lou, S.; Zheng, W.; Qian, Z.; Cui, C.; Zuo, P.; Du, C.; Xie, J.; Wang, J.; Yin, G. Synergistic engineering of defects and architecture in Co<sub>3</sub>O<sub>4</sub>@C nanosheets toward Li/Na ion batteries with enhanced pseudocapacitances. *Nano Energy* **2020**, *78*, 105366, DOI: 10.1016/j.nanoen.2020.105366.
- (38) Zhou, Y.; Wang, C.; Chen, F.; Wang, T.; Ni, Y.; Sun, H.; Yu, N.; Geng, B. Synchronous constructing ion channels and confined space of Co<sub>3</sub>O<sub>4</sub> anode for high-performance lithium-ion batteries. *Nano Research* **2022**, *15*, 6192-6199, DOI: 10.1007/s12274-022-4281-y.
- (39) Wang, L.; Zhang, Z.; Wang, R.; Min, Y.; Cai, J.; Sun, Z. Coordination-assisted fabrication of N-doped carbon nanofibers/ultrasmall Co<sub>3</sub>O<sub>4</sub> nanoparticles for enhanced lithium storage. *J Alloy Compd* **2021**, *855*, 157502, DOI: 10.1016/j.jallcom.2020.157502.
- (40) Li, J.; Yan, D.; Hou, S.; Lu, T.; Yao, Y.; Pan, L. Metal-organic frameworks converted flower-like hybrid with Co<sub>3</sub>O<sub>4</sub> nanoparticles decorated on nitrogen-doped carbon sheets for boosted lithium storage performance. *Chem Eng J* **2018**, *354*, 172-181, DOI: 10.1016/j.cej.2018.08.024.
- (41) Ge, P.; Li, S.; Shuai, H.; Xu, W.; Tian, Y.; Yang, L.; Zou, G.; Hou, H.; Ji, X. Engineering 1D chain-like architecture with conducting polymer towards ultra-fast and high-capacity energy storage by reinforced pseudo-capacitance. *Nano Energy* **2018**, *54*, 26-38, DOI: 10.1016/j.nanoen.2018.09.062.
- (42) Zhang, K.; Xiong, F.; Zhou, J.; Mai, L.; Zhang, L. Universal construction of ultrafine metal oxides coupled in N-enriched 3D carbon nanofibers for high-performance lithium/sodium storage. *Nano Energy* **2020**, *67*, 104222, DOI: 10.1016/j.nanoen.2019.104222.
- (43) Min, J.; Wen, X.; Tang, T.; Chen, X.; Huo, K.; Gong, J.; Azadmanjiri, J.; He, C.; Mijowska, E. A general approach towards carbonization of plastic waste into a well-designed 3D porous carbon framework for super lithium-ion batteries. *Chem Commun (Camb)* **2020**, *56* (64), 9142-9145, DOI: 10.1039/d0cc03236k.
- (44) Wang, F.; Ye, Y.; Wang, Z.; Lu, J.; Zhang, Q.; Zhou, X.; Xiong, Q.; Qiu, X.; Wei, T. MOF-derived Co<sub>3</sub>O<sub>4</sub>@rGO nanocomposites as anodes for high-performance lithium-ion batteries. *Ionics* **2021**, *27* (10), 4197-4204, DOI: 10.1007/s11581-021-04225-4.

- (45) Huang, Y.; Fang, Y.; Lu, X. F.; Luan, D.; Lou, X. W. D. Co<sub>3</sub>O<sub>4</sub> hollow nanoparticles embedded in mesoporous walls of carbon nanoboxes for efficient lithium storage. *Angew Chem Int Ed Engl* **2020**, *59* (45), 19914-19918, DOI: 10.1002/anie.202008987.
- (46) Huang, R.; Li, Y.; Song, Y.; Wang, L. Facial preparation of N-doped carbon foam supporting Co<sub>3</sub>O<sub>4</sub> nanorod arrays as free-standing lithium-ion batteries' anode. *J Alloy Compd* **2020**, *818*, 152839, DOI: 10.1016/j.jallcom.2019.152839.
- (47) Wu, B.; Xie, Y.; Meng, Y.; Qian, C.; Chen, Y.; Yuan, A.; Guo, X.; Yang, H.; Wan, S.; Lin, S. Construction of unique heterogeneous cobalt–manganese oxide porous microspheres for the assembly of long-cycle and high-rate lithium ion battery anodes. *J Mater Chem A* **2019**, *7* (11), 6149-6160, DOI: 10.1039/c8ta09028a.
- (48) Guo, S.; Liu, J.; Zhang, Q.; Jin, Y.; Wang, H. Metal organic framework derived Co<sub>3</sub>O<sub>4</sub>/Co@N–C composite as high-performance anode material for lithium-ion batteries. *J Alloy Compd* **2021**, *855*, 157538, DOI: 10.1016/j.jallcom.2020.157538.
- (49) Mehra, P.; Singh, C.; Cherian, I.; Giri, A.; Paul, A. Deciphering the incredible supercapacitor performance of conducting biordered ultramicroporous graphitic carbon. *ACS Applied Energy Materials* **2021**, *4* (5), 4416-4427, DOI: 10.1021/acsaem.1c00020.
- (50) Guo, K.; Xi, B.; Wei, R.; Li, H.; Feng, J.; Xiong, S. Hierarchical microcables constructed by CoP@C-carbon framework intertwined with carbon nanotubes for efficient lithium storage. *Adv Energy Mater* **2020**, *10*, 1902913, DOI: 10.1002/aenm.201902913.
- (51) Zhang, M.; Deng, Z.-P.; Zhang, X.-F.; Huo, L.-H.; Gao, S. Scallion root biotemplate synthesis of mesoporous Co<sub>3</sub>O<sub>4</sub> hierarchical structure for high capacity and long-lived lithium ion battery anode. *J Alloy Compd* **2021**, *863*, 158772, DOI: 10.1016/j.jallcom.2021.158772.
- (52) Shi, J.; Li, X.; Yang, T.; Tian, X.; Liu, Y.; Lei, S.; Song, Y.; Liu, Z. Co<sub>3</sub>O<sub>4</sub> porous nanorod/N-doped reduced graphene oxide composite with fast pseudocapacitive lithium storage for high-performance lithium-ion capacitors. *J Mater Sci* **2021**, *56* (12), 7520-7532, DOI: 10.1007/s10853-020-05640-0.
- (53) Hu, Y.; Yan, C.; Chen, D.; Lv, C.; Jiao, Y.; Chen, G. One-dimensional Co<sub>3</sub>O<sub>4</sub> nanonet with enhanced rate performance for lithium ion batteries: Carbonyl-β-cyclodextrin inducing and kinetic analysis. *Chem Eng J* **2017**, *321*, 31-39, DOI: 10.1016/j.cej.2017.03.096.
- (54) Ge, Y.; Li, Y.; Wang, F.; Tan, X.; Liu, P.; Wang, D.; Zhou, W.; Yao, Q.; Balogun, M. S.; Huang, D.; Deng, J. Superior high-rate and cycle performances of a single-phase ferrous orthophosphate Na<sub>1.2</sub>Fe<sub>4</sub>(PO<sub>4</sub>)<sub>3</sub> anode material for lithium-ion batteries. *J Power Sources* **2022**, *535*, 231447, DOI: 10.1016/j.jpowsour.2022.231447.
- (55) Xu, X.; Wang, T.; Wen, Y.; Wen, X.; Chen, X.; Hao, C.; Lei, Q.; Mijowska, E. Intumescent flame retardants inspired template-assistant synthesis of N/P dual-doped three-dimensional porous carbons for high-performance supercapacitors. *J Colloid Interface Sci* **2022**, *613*, 35-46, DOI: 10.1016/j.jcis.2022.01.018.
- (56) Yin, M.; Zhao, D.; Feng, C.; Zhou, W.; Jiao, Q.; Feng, X.; Wang, S.; Zhao, Y.; Li, H.; Feng, T. Construction of Porous Co<sub>9</sub>S<sub>8</sub> Hollow Boxes with Double Open Ends toward High-Performance Half/Full Sodium-Ion Batteries. *Acs Sustain Chem Eng* **2020**, *8* (16), 6305-6314, DOI: 10.1021/acssuschemeng.9b07831.